FRICTION PROCESSES IN BRITTLE FRACTURE

BRIAN LAWN
Materials Science and Engineering Laboratory
National Institute of Standards and Technology
Gaithersburg, MD 20899, U.S.A.

ABSTRACT. In this paper we consider the interrelations between friction and fracture in highly brittle materials. First we examine frictional effects in the mechanics of crack formation at elastic and elastic-plastic contacts on brittle surfaces. Then we consider how fundamental intersurface forces manifest themselves as "internal friction" at crack interfaces in "model" solids like mica and glass, with special reference to environmental chemistry. Finally, we examine the controlling role of frictional processes in the strength and toughness of modern ceramic systems.

1. Introduction

Solids with ionic-covalent bonding, "ceramics", are limited in structural applications by one factor, *brittleness*. Such materials, by virtue of their innate inability to sustain energy-absorbing plastic deformation, have a singularly low resistance to the initiation and propagation of cracks. Modern fracture mechanics seeks methodologies for quantifying this brittleness, and, more importantly, of overcoming it [1].

A major player in the fracture properties of brittle ceramics is *friction*. Friction can be *deleterious*, e.g. by augmenting tensile stresses in surface contacts, with adverse effects on strength, abrasion and wear; or *beneficial*, as in toughness, by "shielding" the crack tip and dissipating a portion of the work of applied loading. Its manifestations can be obvious, as in contact configurations, or subtle, as in the crack-tip energy dissipation that attends non-equilibrium fracture in environmentally-assisted crack growth.

We shall illustrate some of the ways friction can play a role in brittle fracture with a selection of examples, drawing from traditional fracture mechanics and modern-day ceramics science.

2. Friction in Contact Fracture

Indentation stress fields usefully simulate real particle contacts in strength degradation, wear and abrasion [2], as depicted in the scheme of fig. 1. In this section we examine some of the indentation crack patterns that form in brittle surfaces, focussing on homogeneous solids like glass and mica. Reference is made to review articles for greater detail [1-4].

In the context of brittle fracture one may usefully classify contacts as "blunt" or

I. L. Singer and H. M. Pollock (eds.), Fundamentals of Friction: Macroscopic and Microscopic Processes, 137–165.

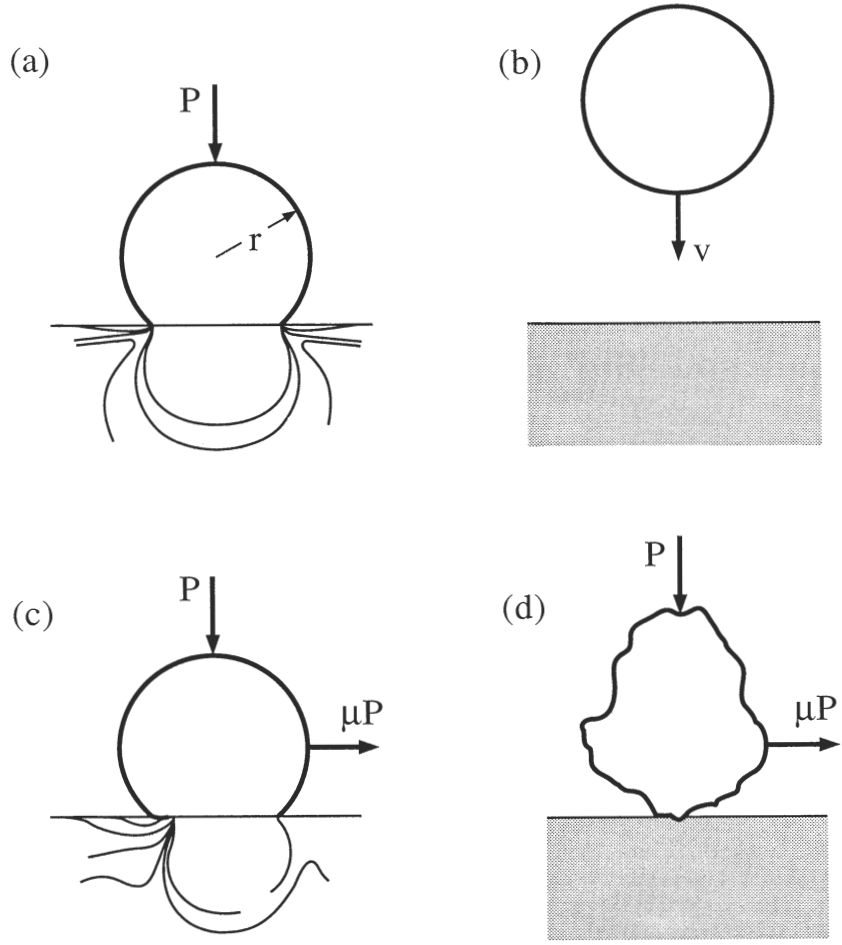

Figure 1. Model for simulating surface damage from particle contact. (a) Static blunt particle (Hertz), sphere radius r and normal load P; (b) impacting sphere, normal velocity v; (c) sliding sphere, with tangential force μP superposed onto normal load P; (d) irregular, sharp sliding particle. Equi-stress contours of tension indicated in (a) and (c).

"sharp". The archetypical *blunt* contact is a sphere on a flat surface in simple Hertzian geometry. The deformation is entirely *elastic* and the ensuing crack at critical loading is the well-documented *Hertzian cone.* Fig. 2 summarises the evolution of this crack type during the indentation loading cycle. *Sharp* contacts are typified by fixed-profile pyramidal indenters, such as the Vickers and Knoop. The deformation is *elastic-plastic*, and the cracks have the *radial* and *lateral* geometry depicted in fig. 3.

2.1 BLUNT CONTACTS AND MODIFIED HERTZIAN CONE CRACKS

The geometrical path and energetics of Hertzian fracture are predetermined by the elastic stress field between two curved surfaces [5]: the crack path by the conical trajectory of maximum tensile stress; the energetics by the subsurface stress falloff along this trajectory.

Initiation. Contact with a sphere of radius r on a flat surface generates tensile stresses on the surface immediately outside the contact circle. These stresses fall off dramatically along the conical path of the prospective crack, fig. 2b. At some point during normal loading P a shallow ring crack develops from a pre-existing surface flaw. With further increase in P the ring extends stably downward until, at a critical load P_C, the ring becomes unstable, and propagates abruptly into the full cone. A detailed fracture mechanics analysis [5] of this instability condition yields

$$P_C = ArR_0 \qquad (1)$$

where $R_0 = 2\gamma$ defines an intrinsic resistance to crack propagation, with γ an appropriate surface energy. The dimensionless coefficient A is the "Auerbach constant", after the discoverer of the empirical relation $P_C \propto r$ one hundred years ago [6]. Whereas satisfaction of Eq. 1 is contingent on the pre-existence of suitable starter microcracks, P_C is (by virtue of the stable growth of the ensuing ring crack) independent of the *initial size* of these microcracks, a prediction borne out by experiments on glass surfaces with controlled, abrasion-induced flaws [7].

Propagation. After propagating downward through the ever-diminishing stress field, the crack arrests in its truncated-cone geometry at a depth $c \approx 3a$ (fig. 2b). The ever-widening circular crack front implies the simple stress-intensity factor relation for penny-like cracks [1]

$$\begin{aligned} K_P &= \chi P/c^{3/2} \\ &= (E'R_0)^{1/2} = T_0 \end{aligned} \qquad (2)$$

where χ is a crack-geometry term and $E' = E/(1 - \nu^2)$, E Young's modulus and ν Poisson's ratio. Eq. 2 is a statement of Griffith equilibrium: the quantity K defines a mechanical driving force on the crack; T_0 defines the intrinsic resistance to crack propagation, or "toughness". The subscript P is to indicate that the stress intensity is operative at maximum load (cf. Eq. 6 below). Thus $c \propto P^{2/3}$, which is the Roesler relation [8] for equilibrium cone cracks. Again, the result is independent of starting flaw size, as expected for a far-field solution.

Friction. The best-studied case of a contact with friction is that of a sliding sphere with complete interfacial slipping, i.e. lateral stress at each element within the contact area equal to friction coefficient μ times normal stress at that element [9]. The effect of

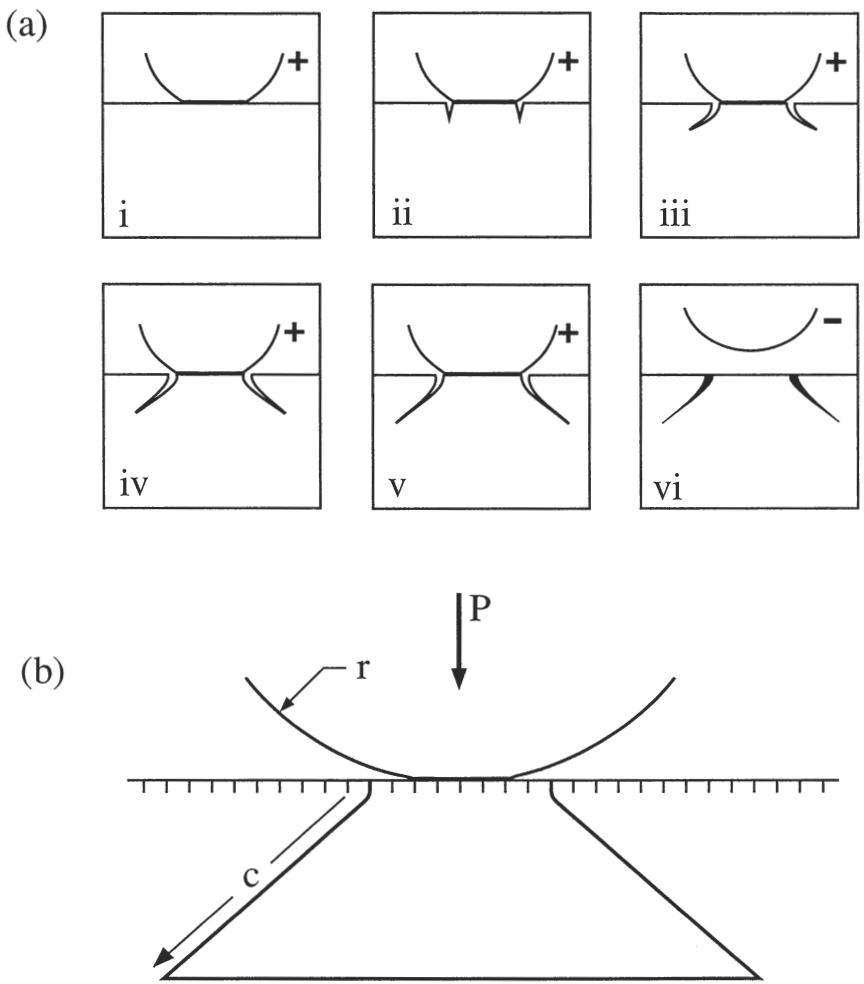

Figure 2. Hertzian cone crack system. (a) Evolution during complete load (+) and unload (-) cycle: (i) preexisting surface flaws experience tensile stresses outside contact circle; (ii) a favourably located flaw runs around contact circle to form a surface ring crack; (iii) at increasing load, the ring crack extends incrementally downward in a rapidly diminishing tensile field; (iv) at critical load the ring becomes unstable and flares downward into the full (truncated) Hertzian cone; (v) at continued loading the arrested cone grows further downward in stable fashion; (vi) at unloading, the cone closes. (b) Essential parameters of system.

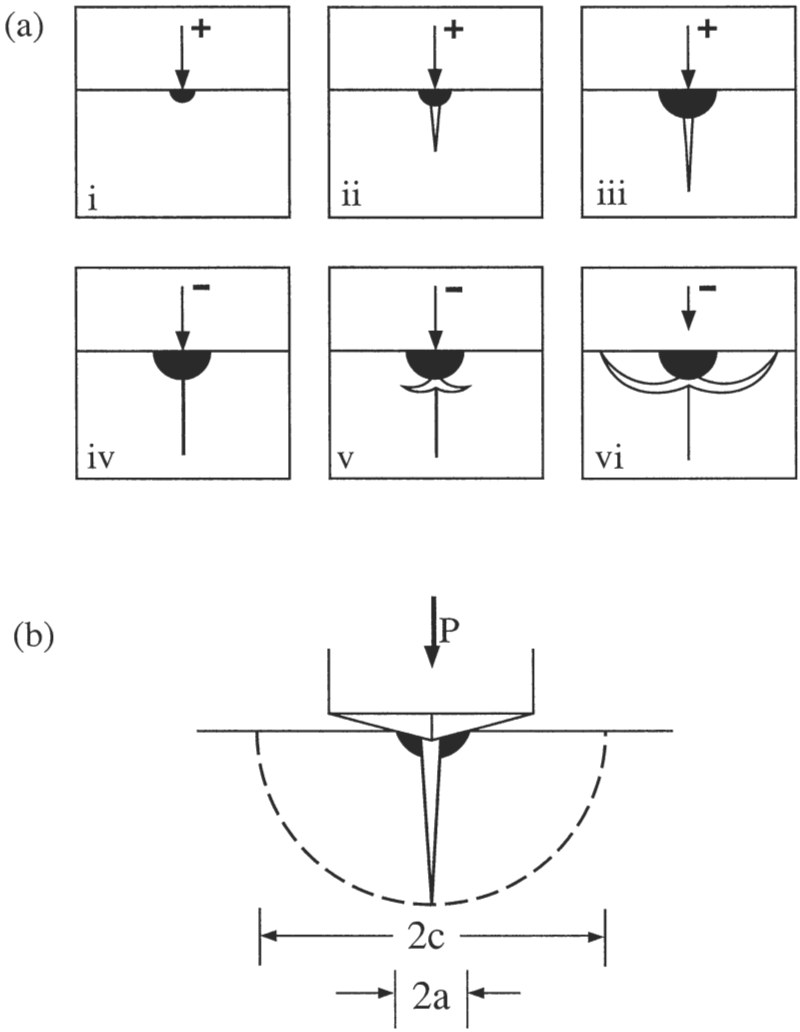

Figure 3. Evolution of radial-lateral crack system during complete load (+) and unload (-) cycle: (i) The sharp point induces plastic deformation; (ii) at critical load shear faults within the deformation zone pop-in to form subsurface radial cracks on median planes; (iii) at increased loading, the radial crack expands further downward; (iv) on initial unloading, the radial cracks expand further, from the action of residual wedge-opening stresses in the near-surface region; (v) at further unloading, the surface radial crack continues to expand, and lateral cracks begin to grow just beneath the free surface; (vi) at full unload, radial and lateral cracks achieve their final, equilibrium penny-like geometry in the residual stress field. (b) Essential parameters of system.

increasing μ is to enhance the tensile field markedly at the trailing edge of the contact, and conversely to suppress it at front, fig. 1c. The critical conditions for crack initiation therefore depend sensitively on the frictional tractions, i.e. $A = A(\mu)$ in Eq. 1 [10,11].

Because of the loss of axial symmetry in the sliding contact stress field the cone cracks are asymmetric and only partially developed [10]. Figure 4 shows cone crack tracks resulting from a steel sphere sliding on glass [12]. Since most of the applied load is supported by the material below the cone frustrum, the resultant geometry may be closely approximated by tilting the cone along the resultant applied load axis, fig. 5 [12]. The magnitude and angular displacement of the load vector in fig. 5 are

$$P = P_N(1 + \mu^2)^{1/2} \tag{3a}$$
$$\beta = \arctan \mu \tag{3b}$$

with P_N the normal component. The crack size is determined from Eqs. 2 and 3 as

$$c = (\chi P_N/T_0)^{2/3}(1 + \mu^2)^{1/3} \tag{4}$$

which is relatively *insensitive* to μ. On the other hand, as is apparent in fig. 4, the *density* of cone cracks increases strongly with μ.

2.2 SHARP INDENTERS AND RADIAL-LATERAL CRACKS

The case of elastic-plastic contact fields in normal loading beneath a sharp pyramidal indenter is more complex. A finite load cannot be supported by an infinitesimal point, so the specimen deforms inelastically at the near-contact. The indenter thereby leaves a permanent impression, the size of which is an (inverse) measure of the hardness.

Initiation. The inelastic deformation strongly influences the ensuing crack pattern by modifying the stress field, generating the radial-lateral crack geometry depicted in fig. 3. The stress intensity about the indenter point approaches the theoretical limit of the structure, causing the material to "fail" along discrete "shear faults" [13,14] in the highly compressive contact near field in order to accommodate the penetrating indenter [15,16]. An example of shear faults at a Vickers indentation in glass is given in fig. 6a. The shear faults, analogous to dislocation slip surfaces in metals but not constrained to crystallographic planes, act as their own sources for subsequent radial and lateral crack "pop-in" - there is no need for pre-existing flaws.

Working models of radial crack initiation [15] treat the faults as shear cracks with restraining interfacial friction, fig. 6b. This interfacial friction persists on unloading the indenter, accounting for the residual impression in brittle materials. The residual impression in turn manifests itself as an outward pressure on the elastic matrix encasing the deformation zone, as represented in "expanding cavity" models of the elastic-plastic field. Radial cracks extend from the ends of the faults at indentation corners, into the outer hoop-tensile field. For fixed-profile indenters (e.g. Vickers) the intensity of the stress field is determined by the size-invariant contact pressure, or "hardness" H. The threshold condition for pop-in is determined as the load at which the shear fault, which scales with the impression diagonal, reaches an unstable size [17,18]:

$$P_C = \Theta T_0(T_0/H)^3 = \Theta E'^2 R_0^2/H^3 \tag{5}$$

with $\Theta = \Theta(E/H)$ a dimensionless coefficient. Hence for sharp indenters the critical load is a strong measure of toughness *and* hardness. The fact that the shear faults act as

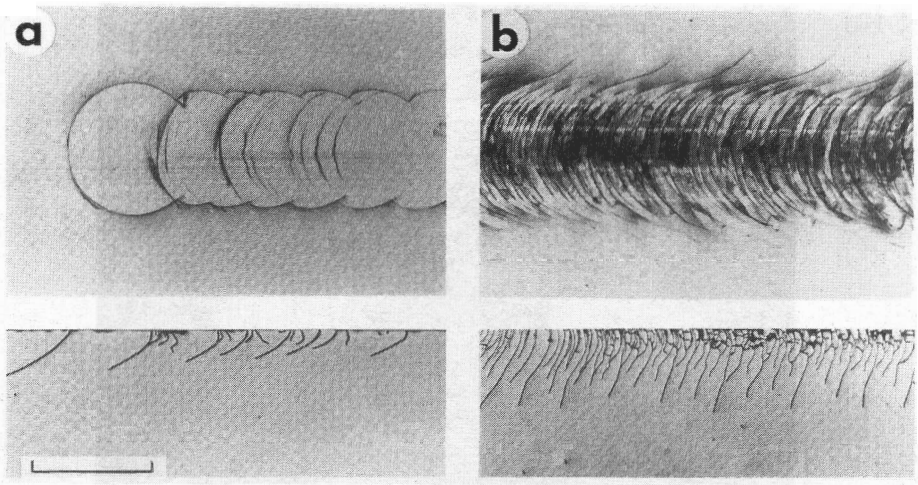

Figure 4. Surface and section views of partial-cone-crack damage on soda-lime glass from sliding steel sphere, r = 3.17 mm, P_N = 20 N: (a) μ = 0.1, (b) μ = 0.5. Index marker 500 μm. From [12].

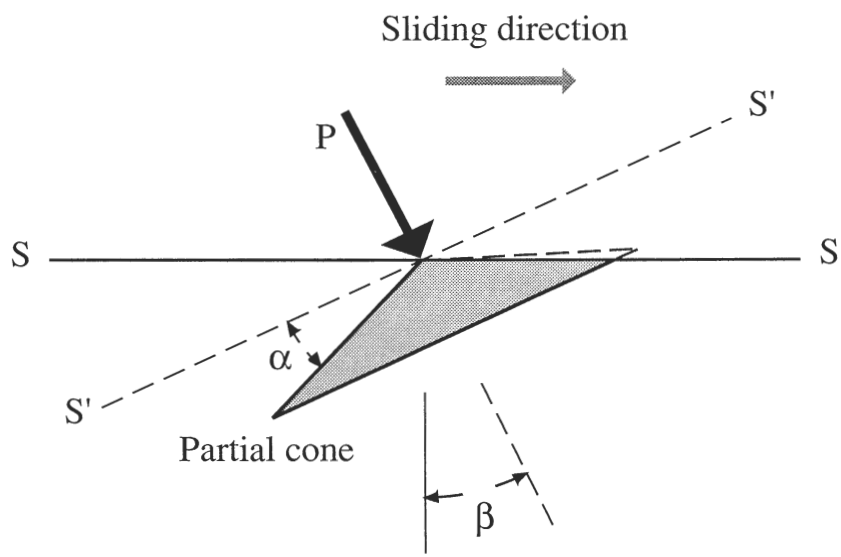

Figure 5. Cone crack geometry for sliding elastic contact of sphere on flat surface. Superposed frictional contact onto normal contact rotates load axis, effectively tilting surface SS (and hence cone axis) through S′S′. Shown here for $\beta = 26.5°$ ($\mu = 0.5$) and $\alpha = 22°$ (glass).

(a)

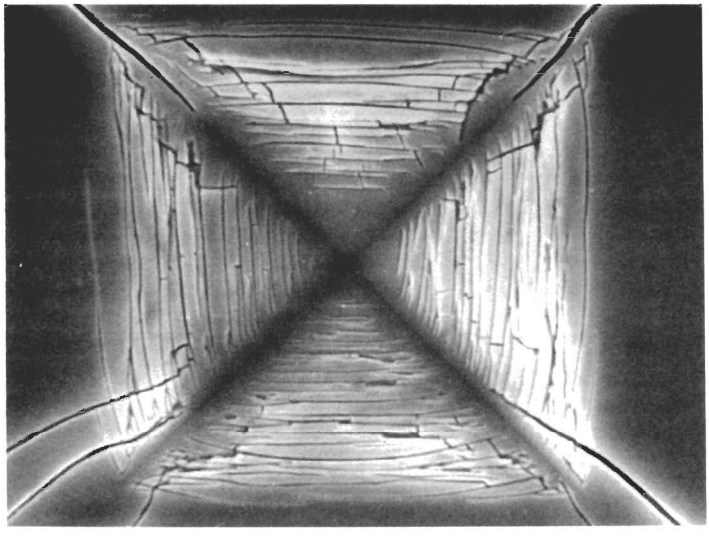

(b)

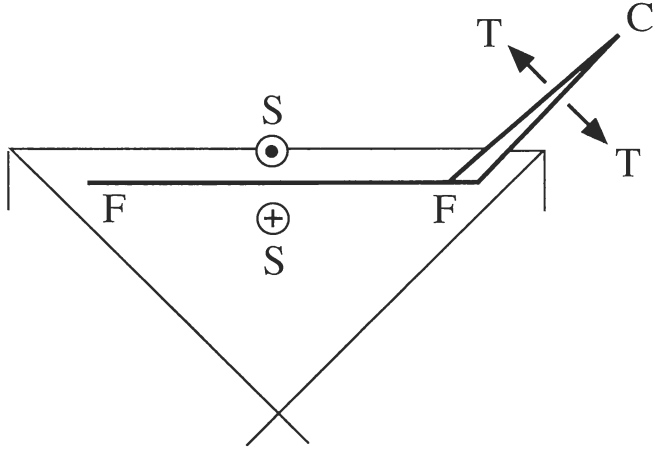

Figure 6. (a) Vickers indentation in soda-lime glass [16]. Surface etched to reveal traces of shear faults, which converge on curved surfaces beneath impression. Width of field 40 μm. (b) Model of radial crack initiation FC from shear fault FF. S denotes frictional shear stresses on fault interface, T tensile stresses in outer residual field.

controlling flaws means that, in contrast to blunt indenters, P_C is the same for pre-damaged and pristine surfaces.

Propagation. On pop-in, the radial and lateral cracks arrest at $c \approx 3a$. Again, both cracks expand on an essentially circular front, so the stress-intensity factor relation for equilibrium "penny-like" cracks is satisfied,

$$K_R = \chi P/c^{3/2} = (E'R_0)^{1/2} = T_0, \quad (6)$$

in analogy to Eq. 2 for blunt indenters. Now, however, the maximum stress intensity is operative in the *unloaded* state - K_R in Eq. 6 relates to the *residual* field in the elastic-plastic contact [19]. The generic relation $c \propto P^{2/3}$ once more holds; and, as in Eq. 4, we expect the modifying effect of contact friction to be weak.

Chemistry. The residual contact field implicit in Eq. 6 can have a profound influence on the crack response in reactive environments. An example is given in Fig. 7. Micrograph (a) shows a radial crack system in glass immediately after completion of contact in inert environment. The residual field is apparent from the persistent birefringence in polarised light. Micrograph (b) shows the same crack pattern after prolonged exposure to laboratory atmosphere. Moisture from the atmosphere diffuses along the crack interface and interacts chemically with the walls in the near-tip region [1,20,21], causing the crack to propagate in a rate-dependent manner. Ultimately, the system reaches a new equilibrium state, determined by the reduced interface energy (Sect. 2.2 below), and the crack comes to rest.

Even more dramatic is the combined effect of residual stress and moisture on radial-crack pop-in. Exposure to water vapour lowers the threshold load for initiation in Eq. 5 relative to inert environments by over two orders of magnitude [15]. Moreover, at intermediate loads the pop-in is "delayed", i.e. occurs spontaneously after completion of the contact cycle.

3. Chemistry in fracture and adhesion

The susceptibility of fracture in brittle solids to environmental interaction raises fundamental questions as to how active species, particularly water, penetrate and interact with crack interfaces. In this section we consider the nature of chemical interactions with intrusive water at fracture interfaces in mica. Mica is an ideal material for fracture studies because of its atomically smooth cleavage, which allows one to study healed as well as virgin interfaces. We emphasise, however, that the behaviour described below is representative of brittle solids in general [1].

3.1 EQUILIBRIUM CRACKS AND ADHESION ENERGIES

The interface adhesion energy (Dupre work of adhesion) for mica interfaces at different relative humidities have been measured in fracture experiments [22-24], using an automated version (fig. 8) of earlier wedge-opening cleavage test arrangements [25,26]. From measurements of crack size c and specimen dimensions one evaluates the mechanical-energy-release rate G (= K^2/E) for double-cantilever specimens [1,22]

$$G = 3Eh^2d^3/4c^4 \quad (7)$$

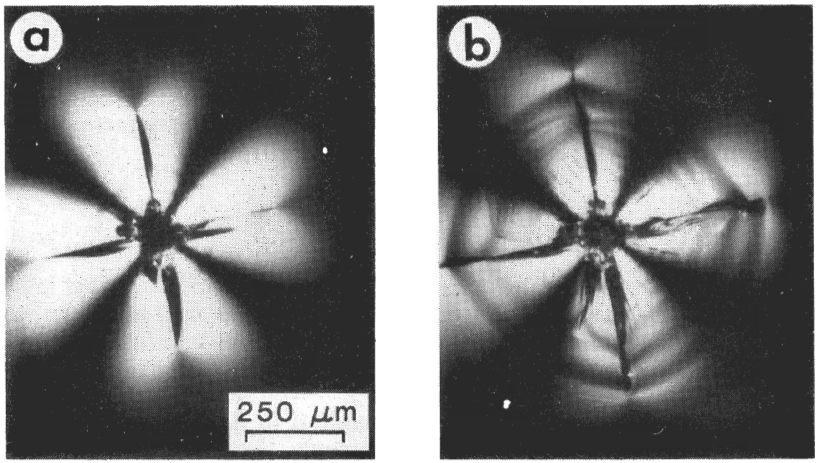

Figure 7. Vickers indentation in soda-lime glass: (a) immediately after completion of contact cycle; (b) same, 1 hr later after exposure to moisture. Note development of both radial and lateral (faint subsurface fringes). Courtesy D.B. Marshall.

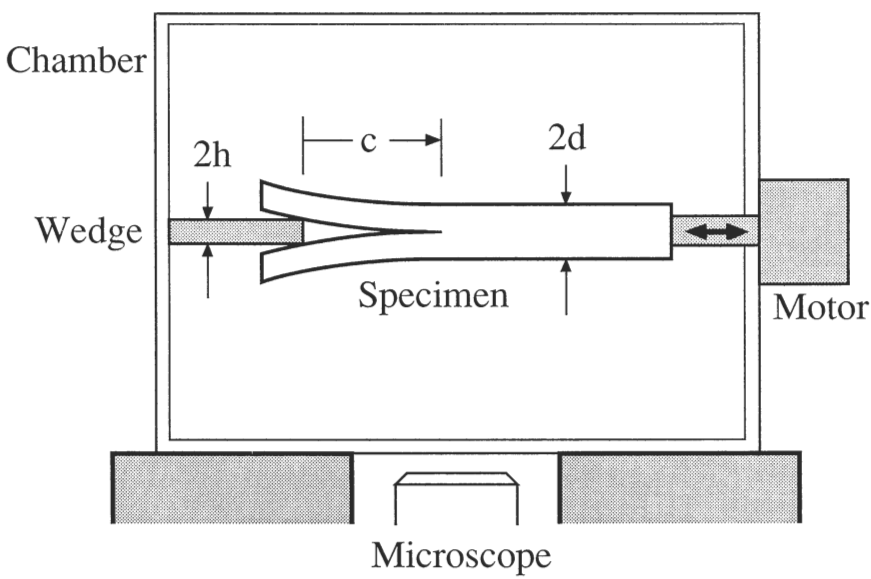

Figure 8. Wedge-opening geometry used to measure adhesion energies and crack velocity curves in mica [22]. Assembly is enclosed in environmental chamber, allowing inert (dry nitrogen gas) and interactive (humid gas) atmospheres. Chamber sits on microscope stage to allow *in situ* viewing (including VCR recording) of crack. Crack motion is effected by translating specimen relative to clamped wedge via stepper motor.

The interface energy is then determined at *Griffith equilibrium*, $G = 2\gamma$. Note $dG/dc < 0$ in Eq. 7, so the equilibrium is stable; i.e. the crack does not go spontaneously to failure as it does in the uniform tensile stress state characteristic of standard strength tests, but advances steadily at constant length c with continued wedge insertion.

Interface energies measured in this way are plotted as a function of relative humidity in fig. 9. Data are included for healed as well as for virgin interfaces. The healed interfaces are obtained by two procedures: the first by simply reversing the wedge motion in an incompletely cleaved specimen, allowing the interface to retain its original coherence; the second by rotating and recontacting fully separated cleavage halves. The primary source of adhesion in the virgin mica is a Coulombic interaction between potassium ions and negative charge in the mica sublayer [27]. Capillary condensation screens these solid-solid electrostatic interactions [28], in the manner of fig. 10 [23,24]. At larger humidities the Kelvin radius of the meniscus, hence the degree of screening, increases until, at saturation, the adhesion is dominated by the Laplace pressure term (equal to twice the surface energy of water - in bulk water even this term is lost). We see that the adhesion is diminished at the healed-coherent interfaces, presumably because of occlusion of water molecules. It is diminished even more at the healed-incoherent (rotated) interfaces, suggesting that loss of lattice registry negates the greater part of the Coulombic interaction [23,24,26].

Some comparative adhesion energy data from pulloff experiments on recontacted mica sheets in the crossed-cylinder configuration of an Israelachvili surface forces apparatus are included in fig. 9. The energies in these experiments were evaluated assuming rigid spheres held together exclusively by capillary action [29]. Maugis [30] has argued that essential complementarity in the macroscopic fracture mechanics exists between brittle-crack and contact-adhesion configurations. In the present case such complementarity applies specifically to the healed-incoherent interfaces, since the opposing mica sheets in the crossed-cylinder geometry are generally recontacted in arbitrary misorientation. That the contact-adhesion data tend to lie below their fracture counterparts in fig. 9, especially at low RH, is attributable in part to failure to account for elastic deformation in the spheres [31,32]. As a final comment concerning the relative merits of brittle-fracture and contact-adhesion methodologies, we note that the former has greater versatility in its capacity to determine the relative influence of lattice registry (healed-coherent vs healed-incoherent interfaces) and occluded water (healed vs virgin interfaces).

Recent experiments on *dis*similar interfaces, e.g. mica-silica, show that the adhesion in dry atmospheres is greatly enhanced by bulk charge transfer across the interface [24,33].

3.2 KINETIC CRACKS AND VELOCITY CURVES

As indicated in Sect. 1.2, brittle cracks exhibit kinetic characteristics in their growth mechanics in reactive atmospheres, with particular sensitivity to water. The *rate* of growth generally increases with increasing displacement of the system from equilibrium. These kinetics are traditionally represented on velocity v-G curves [1,34]. A family of such curves for virgin cracks in mica at different relative humidities is shown in fig. 11. Note that the velocity at each humidity goes rapidly to zero at some "threshold", defined by the equilibrium state $G = 2\gamma$ for that environment (fig. 9).

The micromechanics of rate-dependent crack growth are attributed to diffusion of intrusive species along the crack interface. The atomic structure at the interface near the crack tip provides energy barriers to the diffusion, resulting in energy dissipation by internal friction. Figure 12, computed from linear elasticity solutions for near-tip displacement fields [35], demonstrates how these barriers become less constraining to the penetration of water in mica as G, hence the crack opening, increases. These structure-

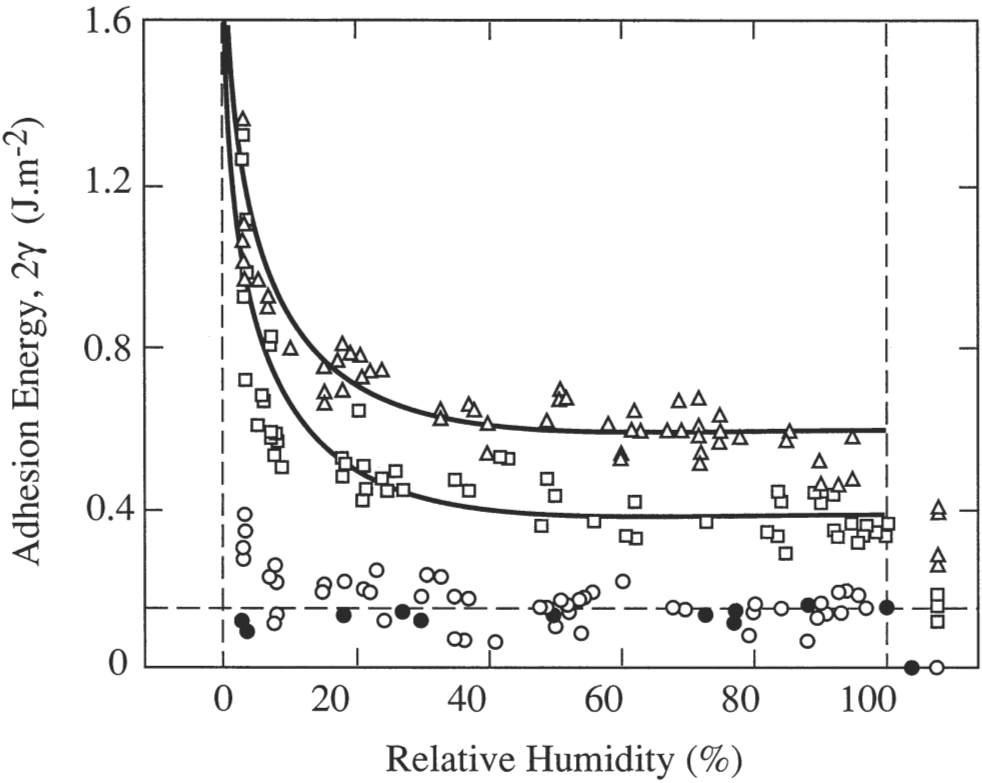

Figure 9. Interface energy of mica as function of relative humidity from fracture experiments. Data for virgin (triangles), healed (squares) and healed-misoriented (circles) interfaces. Points to right of RH 100% correspond to tests in bulk water. Closed symbols are data from Israelachvili-type crossed-cylinder apparatus. Horizontal dashed line denotes capillary contribution, $2\gamma = 144$ mJ·m^{-2} (twice surface tension of water). Solid curves are predictions from theoretical model assuming dielectric screening of solid-solid Coulombic interactions by capillary condensation (fig. 10) [24].

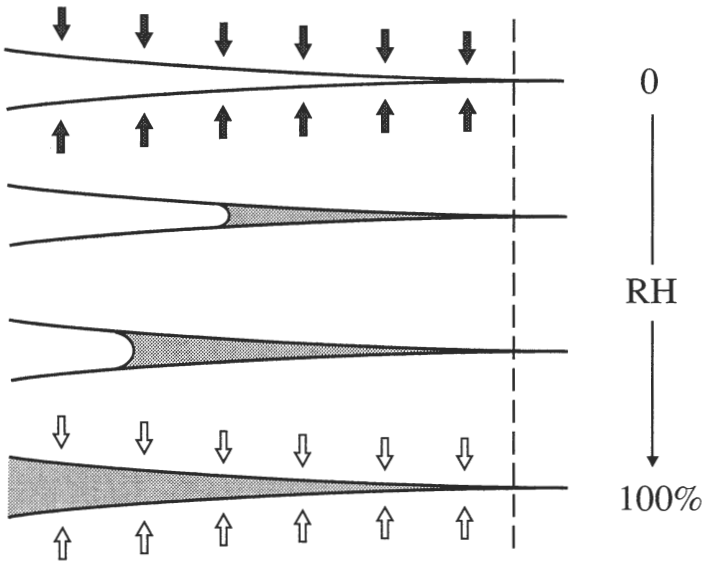

Figure 10. Reduction of interface attraction by capillary condensation. As relative humidity increases, capillary progressively fills crack, replacing strong solid-solid interactions (closed arrows) with weak solid-liquid-solid interactions (open arrows).

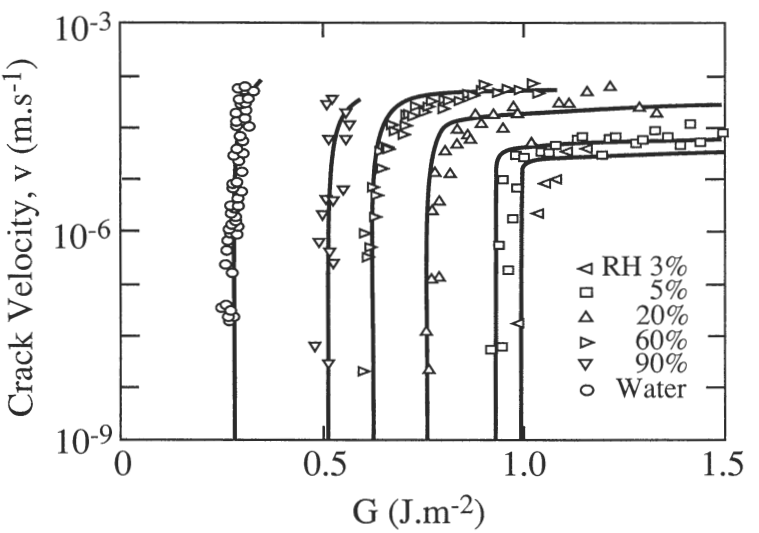

Figure 11. Crack velocity as function of mechanical-energy-release rate for virgin interfaces in mica at specified RH [22].

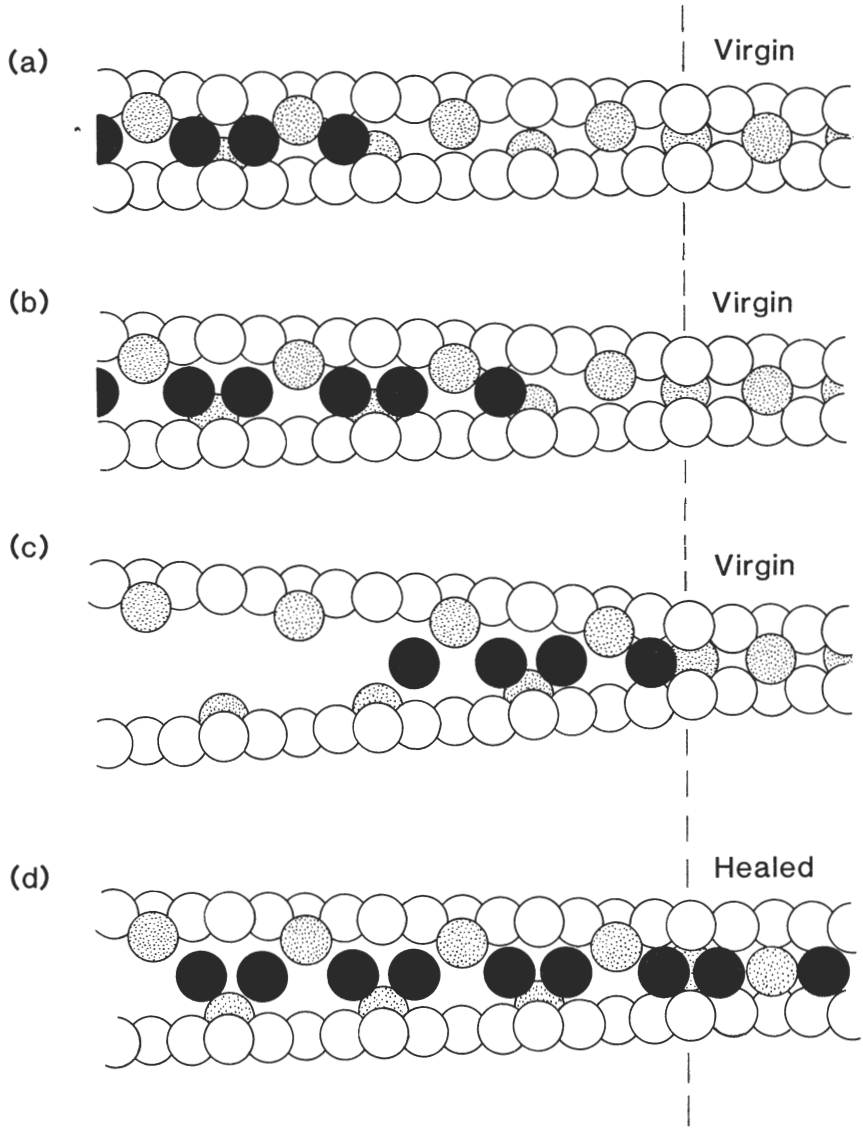

Figure 12. Crack profiles for mica cleavage interfaces [35]. Loading at (a) G = 100 $mJ \cdot m^{-2}$, (b) G = 200 $mJ \cdot m^{-2}$, G = 800 $mJ \cdot m^{-2}$, at virgin interface. Unloading at (d) G = 100 $mJ \cdot m^{-2}$, showing occlusion of intrusive water at healed interface. Elastic sphere representation, with atom sizes from ionic radii and centres from calculated linear elasticity displacement fields. Oxygen - open spheres; potassium - shaded spheres; water - solid spheres.

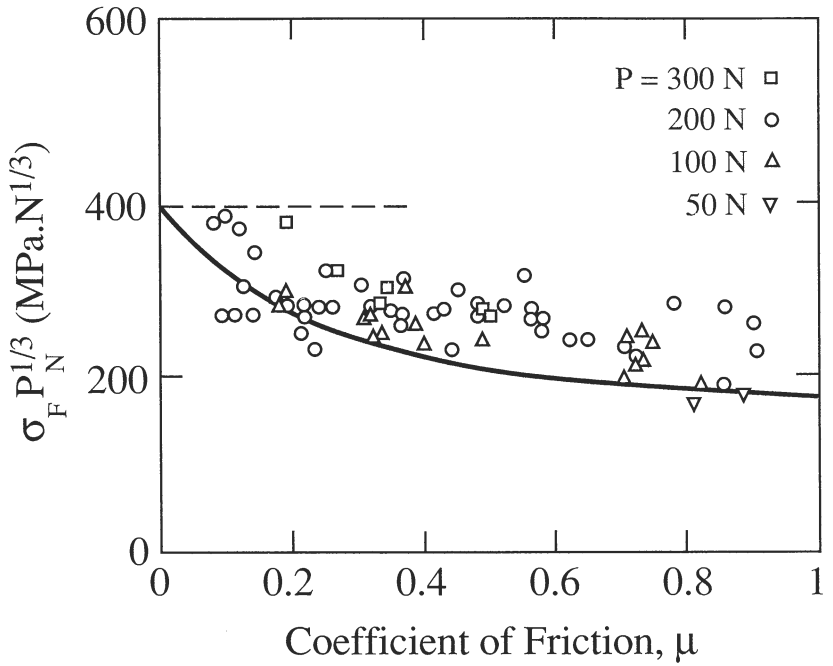

Figure 13. Plot of $\sigma_F P_N^{1/3}$ against μ for glass surfaces subjected to sliding contact with steel sphere at specified loads [12]. Dashed line denotes reference strength level at normal load.

related diffusion barriers are highly sensitive to the crack opening, accounting for the steep velocity increases in fig. 11. At limiting values of G, depending on the humidity, the water vapour can no longer maintain pace with the accelerating tip, and the velocity saturates at the "plateaus" [1,34].

The understanding of velocity curves of the type shown in Fig. 11 is of great practical interest to ceramic engineers who seek methodologies for predicting "lifetimes" of brittle components. In ceramics, flaws as small as 1 μm in inherently unstable stress geometries, i.e. where dK/dc or dG/dc > 0 [1,36], can propagate slowly but decisively to failure at sustained stresses well below the nominal laboratory "inert" strength [37].

4. Friction in strength and toughness of ceramics

Finally, we investigate some practical implications of friction in the strength and toughness properties of modern ceramics. How can we make use of our understanding of contact mechanics and crack-interface energetics in developing brittle materials for structural applications? As we shall show, friction is a critical factor in designing reliable high-toughness materials with strong flaw tolerance.

4.1 STRENGTH DEGRADATION

The strength of brittle surfaces can be severely compromised by the inception of crack-like flaws from contacts with extraneous bodies, of the kind depicted in fig. 1 [38]. Most offensive are the penetrating cone and radial cracks considered in Sect. 1. Friction, by virtue of its enhancement of the contact tensile stresses, is a potentially important player in strength degradation.

Just *how* important friction is depends on whether or not the contact exceeds the threshold for crack initiation. We have already seen in Sect. 1 that the size of well-developed cone or radial cracks is insensitive to μ. We illustrate this insensitivity in fig. 13 with results of strength tests on glass surfaces damaged by sliding spheres under conditions similar to those in fig. 4 [12]. The data are results of strength tests as a function of sliding friction μ, for specified normal loads P_N. The solid curve is a prediction obtained by combining Eq. 4 with the conventional strength equation for failure [1],

$$\sigma_F = T_0/\psi c^{1/2} \tag{8}$$

where $\psi = \psi(\alpha,\beta)$ is a crack geometry factor (fig. 5):

$$\sigma_F P_N^{1/3} = f(\mu)_\alpha T_0^{4/3} \tag{9}$$

with $f(\mu)$ a dimensionless function [12]. We see that σ_F diminishes with μ, but slowly. Hence to the structural engineer who seeks to use ceramic components in mechanical environments where contact-induced cracking is accepted as inevitable (e.g. dust-impacted turbine blades), friction is not a critical design factor.

On the other hand, in ultra-high strength applications where the incidence of a single contact crack is unacceptable, as in freshly-drawn optical glass fibres and polycrystalline ceramics with refined microstructures [1], friction is indeed a critical issue. On such pristine surfaces the spurious contact with a single sharp grit particle as small as 1 μm (fig. 1d) and loads as small as 0.01N (1 g) may be sufficient to reduce the strength of glass by two orders of magnitude [38]. We have already indicated how interfacial friction might play a strong role in enhancing crack pop-in: with blunt indenters, by dramatically diminishing the critical load for cone-crack pop-in (Sect. 1.1); with sharp indenters, via enhanced radial- and lateral-crack initiation from the chemical interaction of moisture at shear-fault interfaces (Sect. 1.2).

4.2 TOUGHNESS

The intrinsic intersurface forces that account for the adhesion energy $G = R_0 = 2\gamma$ in ideally brittle ceramics provide insufficient toughness for most structural applications. The toughness can be raised to an acceptable level only by incorporating highly dissipative elements into the microstructure, thereby introducing an additional component of internal friction [1]. These dissipative elements operate in a "shielding zone" around the crack tip, but do not interact directly with the fundamental bond-separation mode of crack extension. Shielding arises because the dissipative elements effectively oppose the crack opening from the externally applied loads. The most effective form of shielding occurs in metals, via an extensive crack-tip plastic zone. However, there is no analogous dislocation activity at crack tips in ceramics [1,39] (it is this very absence of dislocation activity that gives ceramics their innate brittleness), so other forms of energy dissipation must be sought.

For common polycrystalline ceramics the most effective shielding elements take the form of frictional crack-interface "bridges", e.g. interlocking grain facets, whiskers, fibres.

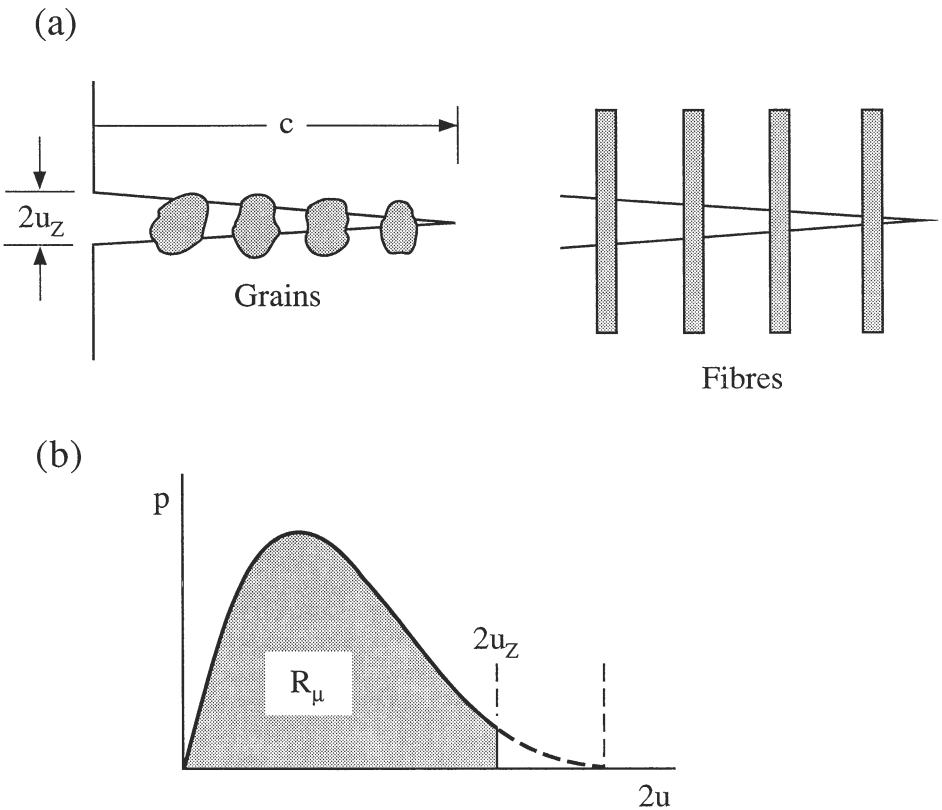

Figure 14. Examples of bridging in ceramic materials. (a) Interlocking grains and embedded fibres. Bridging elements resist crack opening, and thereby "shield" the crack tip from the externally applied loading. (b) Stress-separation function p(u). Area under curve denotes energy absorbed by bridges as they pull out of matrix.

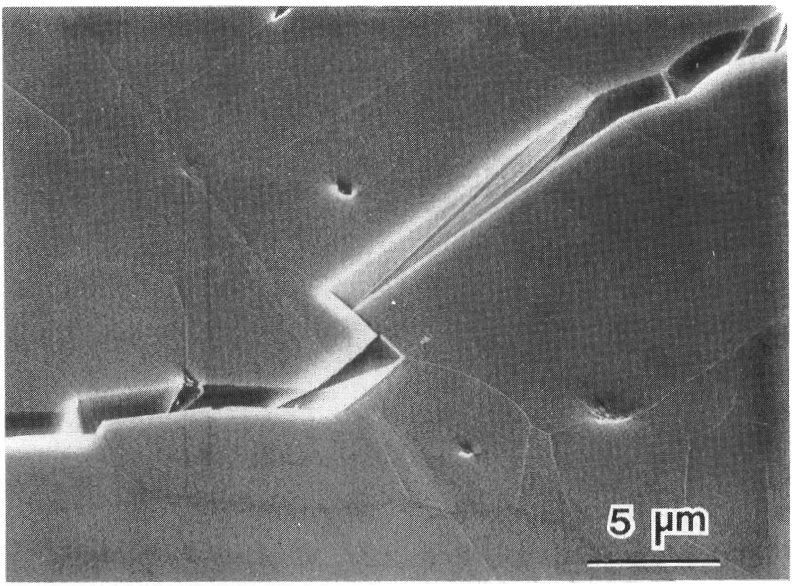

Figure 15. Grain bridging in polycrystalline ceramic. Scanning electron micrograph of crack in alumina, showing facet-facet sliding at interface well behind crack tip [45].

Grain-facet and embedded-fibre bridges are depicted in fig. 14a. The principal requirement for formation of such bridges is that there exist weak grain or interphase boundaries for deflecting the crack [40]. To be effective, the frictional shear stresses τ at these boundaries should be sufficient to dissipate large amounts of energy as the bridging elements pull out. One way of enhancing τ is to build in internal compressive stresses σ_R at the debonding interfaces, giving rise to Coulomb frictional tractions [41]

$$\tau = \mu\sigma_R. \tag{10}$$

The bridging constraint is quantified by a constituent stress-separation function p(u), i.e. restraining stress p exerted by the interfacial elements on the crack walls as a function of crack-opening displacement 2u, as in fig. 14b [1,42,43]. Generally, p is proportional to τ and dependent on characteristic microstructural dimensions like grain size or fibre diameter.

The condition for equilibrium crack extension for a material with bridging becomes

$$G = R_0 + R_\mu = R. \tag{11}$$

The shielding term R_μ is expressible as the area under the stress-separation curve in fig. 14b

$$R_\mu = \int_0^{2u_Z} p(u)du \tag{12}$$

with $2u_z$ the crack opening at the edge of the bridging zone [1,42]. Together with the relation $u_z(c)$, $R_\mu(u_z)$ defines the so-called "R-curve", R(c). The R-curve rises with increasing c from its base level R_0 at c = 0, up to the steady-state level at which the bridging elements ultimately disengage from the crack walls.

4.2.1 *Polycrystalline ceramics*. Grain-facet bridging in polycrystalline ceramics can lead to substantial R-curve behaviour. Typically, for alumina of grain size 25 μm, R increases from a base value 20 $J \cdot m^{-2}$ to a respectable 70 $J \cdot m^{-2}$ over a crack extension 2 mm and crack-opening displacement $2u_z$ = 1 μm [1].

The mechanics of grain bridging have been studied using *in situ* microscopy of crack growth in alumina during loading to failure [44-47]. These observations reveal an extremely interesting failure evolution. The indentation cracks do not remain stationary up to the critical instability stress in the manner of classical Griffith flaws; instead, they grow steadily, grain by grain, for several hundred μm prior to this instability. The flaws are *stabilised* by the rising R-curve.

In addition, the *in situ* observations reveal vital information on the nature of the underlying bridging mechanism [44-47]. Figure 15 shows a micrograph of a bridging site in alumina. Opposing grains remain in intimate sliding contact at adjoining facets across the interface, even though the crack walls have separated through ~10% of the grain diameter, some 1 mm behind the crack tip. High-friction contacts occur principally at those facets under compressive thermal expansion anisotropy stresses in the alumina. The evidence for high frictional stresses is even more vividly demonstrated in cyclic loading, fig. 16 [48]. The cumulation of debris reflects a susceptibility to cyclic *fatigue*, as a progressive degradation of the contacts. The fundamental nature of the friction at the sliding facets has barely been questioned, and leaves us with important material and tribological issues for further study.

The flaw stabilisation from the R-curve manifests itself in a powerful manner in the strength characteristics. The failure condition no longer depends on the *initial* flaw size, but rather on the *extended* flaw size at instability (the "tangency point" on the R-curve [1,36]). Hence materials with pronounced R-curves tend to be *flaw tolerant*. To enhance this flaw tolerance we need to increase the area under the p(u) curve in fig. 14b. One way of doing this is to enhance the friction stress in Eq. 10, via σ_R, by incorporating a second phase with large differential expansion coefficients relative to the matrix [49]. Aluminum titanate is a prime candidate in alumina matrices: its c-axis coefficient is -3×10^{-6} °C^{-1} compared to 10×10^{-6} °C^{-1} for alumina. Figure 17 shows how incorporation of 20% aluminum titanate into a 6 μm alumina matrix produces a striking improvement in flaw insensitivity. Such flaw insensitivity is of intense interest to ceramicists: to the engineer, for the potential to design to a well-defined stress level, with greatly reduced susceptibility to subsequent in-service damage and with a built-in stable crack growth system to warn of imminent failure; and to the processor, for tailoring materials with specifiable properties for specific applications.

4.2.2 *Fibre-reinforced ceramics*. As with polycrystalline ceramics, the toughness of ceramic-matrix composites reinforced with fibres is controlled largely by interfacial friction properties. Accordingly, much effort is being devoted by the ceramics community to the measurement of friction in "pull-out" or "push-in" tests. In the *push-in* test, friction stresses are evaluated by measuring the hysteresis in the load-displacement function through one cycle [50].

A recent variant on the *pull-out* test has provided a vital clue as to the nature of friction in some fibre-composite systems [51,52]. A fibre protruding from both faces of a matrix section is pulled axially until it debonds and slips steadily through the section.

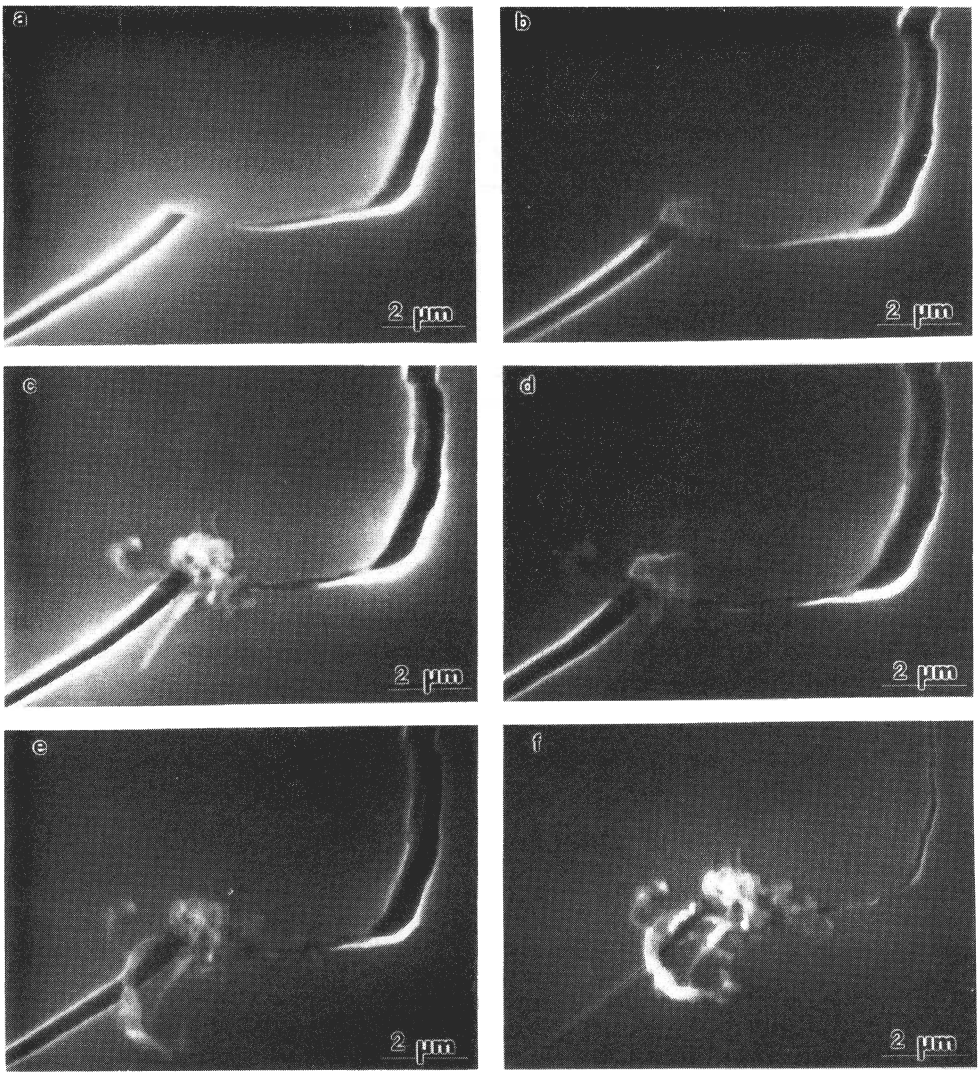

Figure 16. Scanning electron micrograph of frictional grain facet in alumina at sequential stages of cycling [48]. At maximum load, after: after (a) 0, (b) 7000, (c) 20000, (d) 27000, (e) 45000 cycles. After complete unload, (f). Note cumulation of frictional debris at facet.

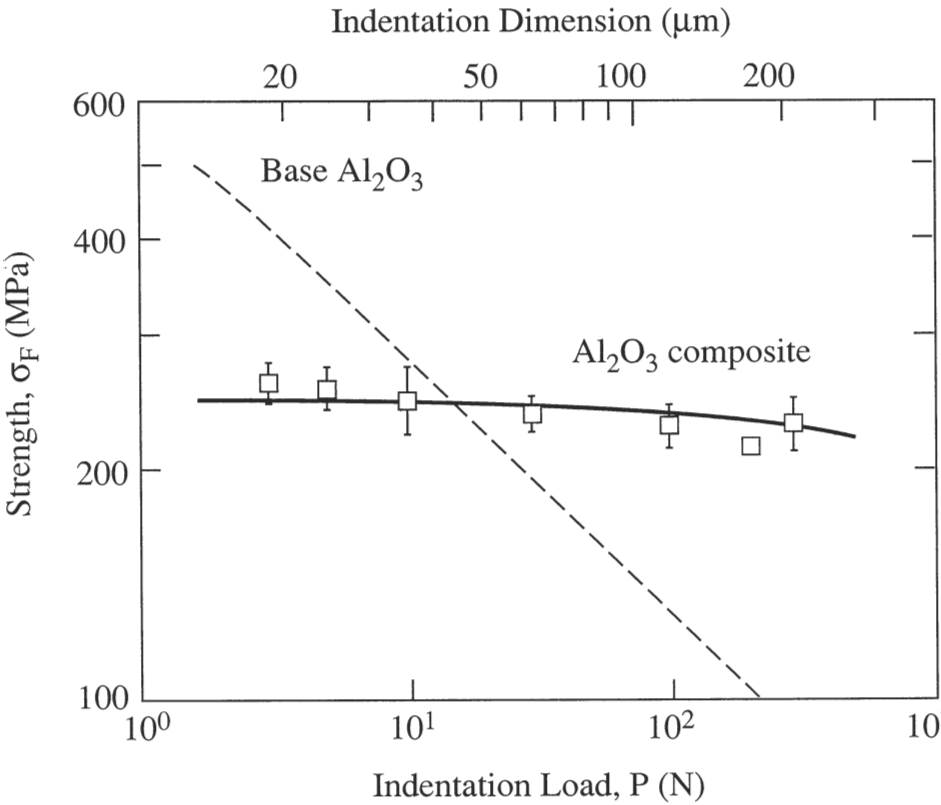

Figure 17. Strength of alumina matrix composite (grain size 6 μm) with aluminium titanate phase, as function of indentation load and flaw size (indentation diagonal). Dashed curve denotes behaviour for base alumina matrix. Note strongly enhanced flaw tolerance. After [49].

Before pull-through is complete the specimen is inverted and the fibre pulled back in the opposite direction. Figure 18 shows the two load-displacement half-cycles for a silicon carbide fibre in a borosilicate matrix. The steep rise in the curve at left reflects the initial debonding and fibre unseating as a shear crack spreads along the interface. At full debonding through the section the entire fibre, after some stick-slip, begins to pull out steadily. The relatively flat curve at right in fig. 18 indicates a steady reverse friction until, at the original fibre location, the system exhibits an abrupt reseating drop. This last feature, first reported by Jero and Kerans [51] in push-in tests, immediately suggests that there is a strong surface roughness component in the friction characteristic.

A detailed asperity model accounting for this surface roughness has been advanced [52]. Essential details are shown in fig. 19. A random distribution of spherical elastic asperities is presumed to exist on both fibre and matrix surfaces, so that interfacial contact is made through a distribution of Hertzian junctions. Microscopic examination of pulled-

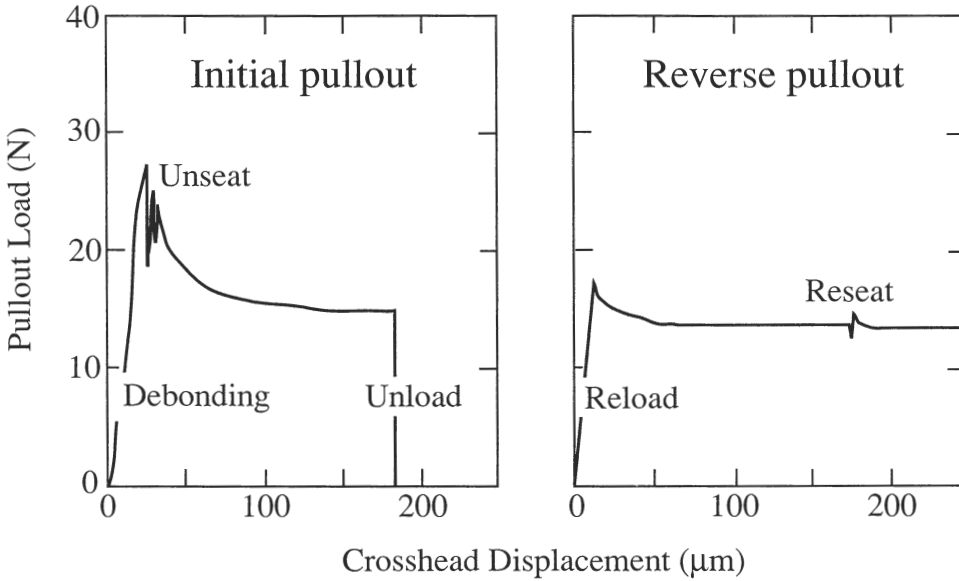

Figure 18. Measured force-displacement data for pullout of SiC fibre from borosilicate glass matrix [52]. *Left curve*, first pullout. *Right curve*, reverse pullout. Note initial steep peak at extreme left, and load drop at extreme right.

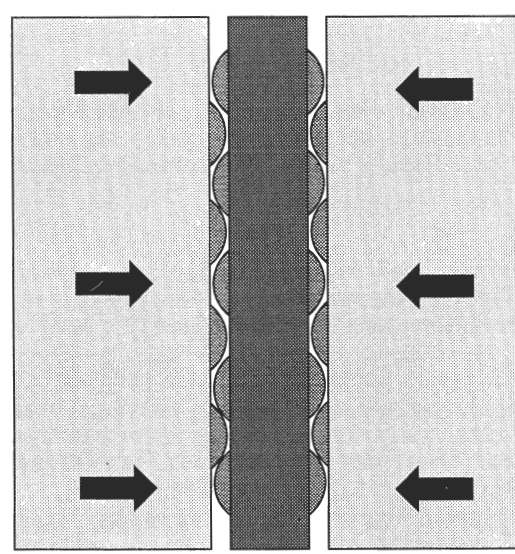

Figure 19. Asperity model of fibre pullout [52]. Asperities are treated as Hertzian contacts, under compressive loading from thermal mismatch stresses.

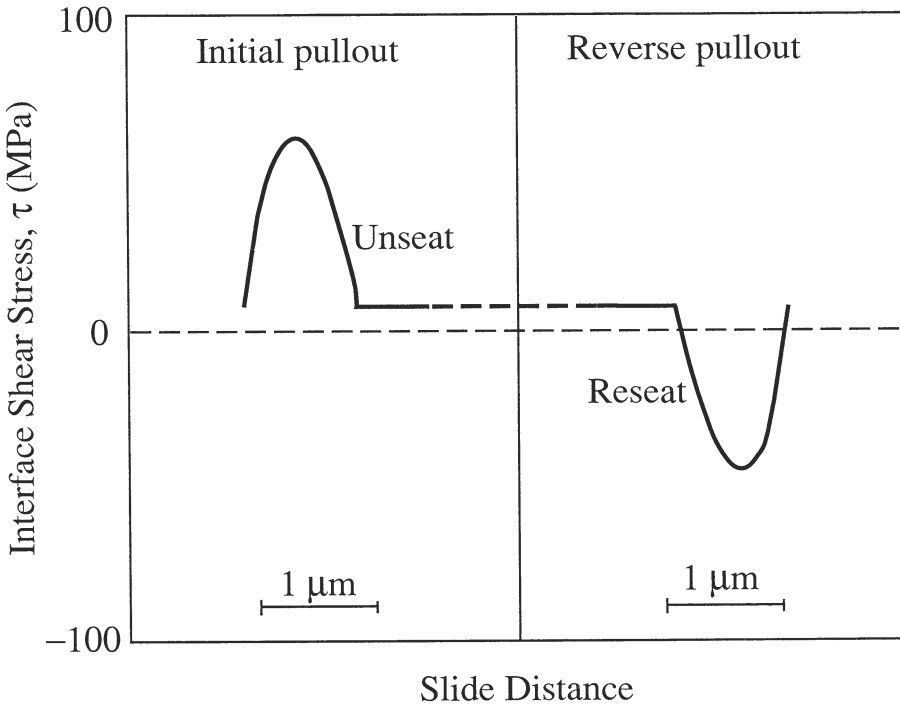

Figure 20. Calculated interfacial shear stress as function of sliding distance for model in fig. 19. Maximum at left indicates correlated elastic forces opposing unseating of asperities from their original interlock configuration. Corresponding minimum at right indicates reseating on reversed pullout. Cf. fig. 18. From [52].

out fibre surfaces confirms the existence of such asperities. In the original state the junctions of one surface seat in the valleys of the other, clamped by thermal mismatch stresses. The calculated shear resistance stress τ, using measured asperity dimensions and elastic parameters characteristic of the SiC/glass fiber-matrix system described above, is plotted as a function of fibre displacement in fig. 20. This plot reflects the broader features of the experimental pullout-displacement function in fig. 18. The initial resistance is large because of increasing resistance from both elastic deformation and the associated friction, accounting for the load peak at left. Once the asperities reach the first summits of their opposing counterparts the local normal components of the randomised Hertzian contacts average out to zero over the interface, leaving only the friction components, which always act in concert to oppose subsequent motion. The net friction thereafter maintains its steady-state value as sliding proceeds. This value is the same on reversing the pullout (albeit with opposite sign) until, ultimately, the asperities reseat and the system experiences the load drop.

5. Conclusions

(i) Contact fracture is influenced by friction at the loading interface, propagation less so than initiation. Indenters may be classified as "blunt" (elastic) or "sharp (elastic-plastic). The latter are characterised by strong residual stress fields.

(ii) Brittle fracture is chemistry-enhanced. Fracture and adhesion are governed by intersurface forces, which may be profoundly weakened by intervening fluid species (especially water). Interface energies determine equilibrium states, interfacial diffusion barriers kinetic states.

(iii) Friction is an important element in designing with structural ceramics. Strength is degraded by friction, less so in the domain of propagation than of initiation. Toughness is enhanced by friction at interfaces between microstructural elements in ceramic systems.

Acknowledgements

The author acknowledges many discussions and valuable contributions on various facets of this work with S.J. Bennison, L.M. Braun, E.P. Butler, E.R. Fuller, R.G. Horn, P.D. Jero, R.J. Kerans, S. Lathabai, J. Rödel, D.T. Smith, K-T. Wan. Funding was provided by the U.S. Office of Naval Research.

References

1. B.R. Lawn (1992). "Fracture of Brittle Solids". Cambridge University Press, Cambridge.
2. B.R. Lawn and T.R. Wilshaw (1975) "Indentation Fracture: Principles and Applications", *J. Mater. Sci.* **10** 1049-81.
3. A.G. Evans and T.R. Wilshaw (1976) "Quasi-Static Solid Particle Damage in Brittle Solids", *Acta Metall.* **24** 939-56.
4. B.R. Lawn and S.M. Wiederhorn (1983), "Contact Fracture in Brittle Materials", in Contact Mechanics and Wear of Rail/Wheel Systems", pp. 133-47, ed. J. Kalousek, R.V. Dukkipati and G.M. Gladwell. University of Waterloo Press, Vancouver.
5. F.C. Frank and B.R. Lawn (1967) "On the Theory of Hertzian Fracture", *Proc. Roy. Soc. Lond.* **A299** 291-306.
6. F. Auerbach (1891) "Measurement of Hardness", *Ann. Phys. Chem.* **43** 61-100.
7. F.B. Langitan and B.R. Lawn (1969) "Hertzian Fracture Experiments on Abraded Glass Surfaces as Definitive Evidence of Auerbach's Law", *J. Appl. Phys.* **40** 4009-17.
8. F.C. Roesler (1956) "Brittle Fractures Near Equilibrium", *Proc. Phys. Soc. Lond.* **B69** 981-92.
9. G.E. Hamilton and L.E. Goodman (1966) "The Stress Field Created by a Sliding Contact", *J. Appl. Mech.* **33** 371-76.
10. B.R. Lawn (1967) "Partial Cone Crack Formation in a Brittle Material Loaded with a Sliding Spherical Indenter", *Proc. Roy. Soc. Lond.* **A299** 307-16.
11. D.R. Gilroy and W. Hirst (1969) "Brittle Fracture of Glass Under Normal and Sliding Loads", *Brit. J. Appl. Phys.* **2** 1784-87.

12. B.R. Lawn, S.M. Wiederhorn and D.E. Roberts (1984), "Effect of Sliding Friction Forces on the Strength of Brittle Materials", *J. Mater. Sci.* **19** 2561-69.
13. J.T. Hagan and M.V. Swain (1976) "Indentation Plasticity and the Ensuing Fracture of Glass", *J. Phys. D: Appl. Phys.* **9** 2201-14.
14. J. Hagan (1980) "Shear Deformation Under Pyramidal Indentations in Soda-Lime Glass, *J. Mater. Sci.* **15** 1417-24.
15. B.R. Lawn, T.P. Dabbs and C.J. Fairbanks (1983) "Kinetics of Shear-Activated Crack Initiation in Soda-Lime Glass", *J. Mater. Sci.* **18** 2785-97.
16. T.P. Dabbs, C.J. Fairbanks and B.R. Lawn (1984) "Subthreshold Indentation Flaws in the Study of Fatigue Properties of Ultrahigh Strength Glass", in Methods for Assessing the Strength and Reliability of Brittle Materials, pp. 142-52, ed. S.W. Freiman and C.M. Hudson. A.S.T.M. Special Technical Publication **844**, Philadelphia.
17. B.R. Lawn and A.G. Evans (1977) "A Model for Crack Inititation in Elastic/Plastic Indentation Fields", *J. Mater. Sci.* **12** 2195-99.
18. K. Puttick (1980) "The Correlation of Fracture Transitions", *J. Phys. D: Appl. Phys.* **13** 2249-62.
19. B.R. Lawn, A.G. Evans and D.B. Marshall (1980), "Elastic/Plastic Indentation Damage in Ceramics: The Median/Radial Crack System", *J. Amer. Ceram. Soc.* **63** 574-81.
20. S.M. Wiederhorn (1967) "Influence of Water Vapor on Crack Propagation in Soda-Lime Glass", *J. Amer. Ceram. Soc.* **50** 407-14.
21. S.M. Wiederhorn and L.H. Bolz (1970) "Stress Corrosion and Static Fatigue of Glass", *J. Amer. Ceram. Soc.* **53** 543-48.
22. K-T. Wan, N. Aimard, S. Lathabai, R.G. Horn and B.R. Lawn (1990) "Interfacial Energy States of Moisture-Exposed Cracks in Mica", *J.Mater. Res.* **5** 172-82.
23. K-T. Wan and B.R. Lawn (1990) "Surface Forces in Mica in the Presence of Capillary Condensation", *Acta Metall.* **38** 2073-83.
24. K-T. Wan, D.T. Smith and B.R. Lawn (1992) "Contact and Adhesion Energies of Mica-Mica, Silica-Silica and Mica-Silica Interfaces in Dry and Moist Atmospheres", *J. Amer. Ceram. Soc.*, in press.
25. J.W. Obreimoff (1930) "The Splitting Strength of Mica", *Proc. Roy. Soc. Lond.* **A127** 290-97.
26. A.I. Bailey and S.M. Kay (1967) "A Direct Measurement of the Influence of Vapour, of Liquid and of Oriented Monolayers on the Interfacial Energy of Mica", *Proc. Roy. Soc. Lond.* **A301** 3421-27.
27. S.W. Bailey (1984) "Review of Cation Ordering in Micas", *Clays and Clay Minerals* **32** 81-92.
28. G.L. Gaines and D. Tabor (1956) "Surface Adhesion and Elastic Properties of Mica", *Nature* **178** 1304-05.
29. H. Christenson (1988) "Adhesion Between Surfaces in Undersaturated Vapours - A Reexamination of the Influence of Meniscus Curvature and Surface Forces", *J. Colloid Interf. Sci.* **121** 170-78.
30. D. Maugis (1985) "Subcritical Crack Growth, Surface Energy, Fracture Toughness, Stick-Slip and Embrittlement", *J. Mater. Sci.* **20** 3041-73.
31. A. Fogden and L.R. White (1990) "Contact Elasticity in the Presence of Capillary Condensation: I. The Nonadhesive Hertz Problem", *J. Colloid Interf. Sci.* **138** 414-30.
32. D. Maugis (1991) "Adhesion of Spheres: the JKR-DMT Transition Using a Dugdale Model", *J. Colloid Interf. Sci.***150**, 243-269.

33. D.T. Smith and R.G. Horn, "The Effect of Charge Transfer on the Adhesion Between Dissimilar Materials", in preparation.
34. K-T. Wan, S. Lathabai and B.R. Lawn (1990) "Crack Velocity Functions and Thresholds in Brittle Solids", *J. Europ. Ceram. Soc.* **6** 259-68.
35. B.R. Lawn, D.H. Roach and R.M. Thomson (1987) "Thresholds and Reversibility in Brittle Cracks: An Atomistic Surface Force Model", *J. Mater. Sci.* **22** 4036-50.
36. Y-W. Mai and B.R. Lawn (1986) "Crack Stability and Toughness Characteristics in Brittle Materials", *Ann. Rev. Mater. Sci.* **16** 415-39.
37. J.E. Ritter (1974) "Engineering Design and Fatigue Failure of Brittle Materials", in Fracture Mechanics of Ceramics, Vol. 4, pp. 667-86, ed. R.C. Bradt, D.P.H. Hasselman and F.F. Lange. Plenum Press, New York.
38. B.R. Lawn, D.B. Marshall, P. Chantikul and G.R. Anstis (1980) "Indentation Fracture: Applications in the Assessment of Strength of Ceramics", *J. Aust. Ceram. Soc.* **16** 4-9.
39. B.R. Lawn, B.J. Hockey and S.M. Wiederhorn (1980) "Atomically Sharp Cracks in Brittle Solids: An Electron Microscopy Study", *J. Mater. Sci.* **15** 1207-23.
40. J. Cook and J.E. Gordon (1964) "A Mechanism for the Control of Crack Propagation in all Brittle Systems", *Proc. Roy. Soc. Lond.* **A282** 508-20.
41. S.J. Bennison and B.R. Lawn (1989) "Role of Interfacial Grain-Bridging Sliding Friction in the Crack-Resistance and Strength Properties of Nontransforming Ceramics", *Acta Metall.* **37** 2659-71.
42. A.G. Evans (1990) "Perspectives on the Development of High-Toughness Ceramics", *J. Amer. Ceram. Soc.* **73** 187-206.
43. Y-W. Mai and B.R. Lawn (1987) "Crack-Interface Grain Bridging as a Fracture Resistance Mechanism in Ceramics: II. Theoretical Fracture Mechanics Model", *J. Amer. Ceram. Soc.* **70** 289-94.
44. F. Deuerler, R. Knehans and R. Steinbrech (1986) "Testing Methods and Crack-Resistance Behaviour of Al_2O_3", *J. de Physique* **C1** 617-20.
45. P.L. Swanson, C.J. Fairbanks, B.R. Lawn, Y-W. Mai and B.J. Hockey (1987) "Crack-Interface Grain Bridging as a Fracture Resistance Mechanism in Ceramics: I. Experimental Study on Alumina", *J. Amer. Ceram. Soc.* **70** 279-89.
46. J. Rödel, J. Kelly and B.R. Lawn (1990) "In Situ Measurements of Bridged Cracks Interfaces in the SEM", *J. Amer. Ceram. Soc.* **73** 3313-18.
47. G. Vekinis, M.F. Ashby and P.W.R. Beaumont (1990) "R-Curve Behaviour of Al_2O_3Ceramics", *Acta Metall.* **38** 1151-62.
48. S. Lathabai, J. Rödel and B.R. Lawn (1991) "Cyclic Fatigue From Frictional Degradation at Bridging Grains in Alumina", *J. Amer. Ceram. Soc.* **74** 3340-48.
49. S.J. Bennison, J. Rödel, S. Lathabai and B.R. Lawn (1991) "Microstructure, Toughness Curves and Mechanical Properties of Alumina Ceramics", in Toughening Mechanisms in Quasi-Brittle Materials, pp. 209-33, ed. S.P. Shah. Kluwer Academic Publishers, Dordrecht, the Netherlands.
50. D.B. Marshall (1984) "An Indentation Method for Measuring Matrix-Fiber Frictional Stresses in Ceramic Composites", *J. Amer. Ceram. Soc.* **67** C259-60.
51. P.D. Jero and R.J. Kerans (1991) "Effect of Interface Roughness on the Frictional Shear Stress Measured Using a Pushout Test", *J. Amer. Ceram. Soc.*, in press.
52. E.R. Fuller, E.P. Butler and W.C. Carter (1991) "Determination of Fiber-Matrix Interfacial Properties of Importance to Ceramic Composite Toughening", in Toughening Mechanisms in Quasi-Brittle Materials, pp. 385-403, ed. S.P. Shah. Kluwer Academic Publishers, Dordrecht, the Netherlands.